Biochemical and Biophysical Research Communications 827 (2026) 154059

Contents lists available at ScienceDirect

Biochemical and Biophysical Research Communications

journal homepage: www.elsevier.com/locate/ybbrc

Electrostatic control of membrane disruption and amorphous coaggregation by dynorphin A variants

Mohsen Habibnia [a,b], Eric Catalina-Hernandez [a,b], Ramon Barnadas-Rodríguez [a,b], Alex Peralvarez-Marin [a,b,*]

[a] Unit of Biophysics, Department of Biochemistry and Molecular Biology, Facultat de Medicina, Universitat Autònoma de Barcelona, Av. Can Domènech s/n, Cerdanyola del Vallès, Catalonia, 08193, Spain
[b] Institute of Neurosciences, Universitat Autònoma de Barcelona, Cerdanyola del Vallès, Catalonia, 08193, Spain

ARTICLE INFO

Keywords:
Dynorphins
Membrane disruption
Molecular dynamics simulations
Liposome leakage
Membrane composition

ABSTRACT

Dynorphin A is a highly cationic neuropeptide that exhibits membrane activity beyond its canonical opioid receptor signaling. Here, we investigate how sequence variants of Dynorphin A associated with spinocerebellar ataxia type 23 modulate membrane disruption and aggregation behavior. Using computational electrophysiology simulations combined with liposome leakage and fluorescence-based aggregation assays, we show that Dynorphin A variants interact with lipid bilayers primarily via electrostatic recruitment, followed by mutation-dependent insertion and transient pore formation. Anionic lipids promote bilayer disruption, while cholesterol attenuates peptide activity in a variant-specific manner. Although Dynorphin A variants do not spontaneously form ordered aggregates, they markedly alter amyloid-β co-assembly by enhancing hydrophobic surface exposure without proportionally increasing fibrillization. These results demonstrate that subtle sequence changes fine-tune the balance between membrane perturbation and amorphous co-aggregation, and highlight electrostatic membrane recruitment as a key determinant of DynA bioactivity.

1. Introduction

Dynorphins are among the most positively charged peptides in the human body [1] and constitute a major family of endogenous opioid peptides. They are derived from the prodynorphin (PDYN) precursor [2], which undergoes proteolytic processing at basic residues to generate Big Dynorphin (BigDyn, 32 residues) and, subsequently, Dynorphin A (DynA, residues 1–17) and Dynorphin B (DynB, residues 20–32) following cleavage at the K–R hinge region [3,4]. Dynorphins act primarily as agonists of κ-opioid receptors (KOR) and, to a lesser extent, μ-opioid receptors (MOR), contributing to analgesia, stress responses, and addiction-related behaviors [5].

In addition to their canonical receptor-mediated activity, DynA displays a second, non-classical mode of action involving direct interactions with lipid membranes. Multiple studies have shown that DynA can disrupt membrane integrity independently of opioid receptor activation[6–10]. These membrane-active properties have been implicated in neurological disorders, including Spinocerebellar Ataxia Type 23 (SCA23) [11,12]. Mutations in the PDYN gene associated with SCA23 specifically alter the DynA sequence [8,13,14], giving rise to four clinically relevant variants: wild-type DynA (WT), a leucine-to-serine substitution at position 5 (L5S), an arginine-to-tryptophan substitution at position 6 (R6W), and an arginine-to-cysteine substitution at position 9 (R9C).

Previous work has demonstrated that DynA behaves as a cell-penetrating peptide (CPP), capable of translocating across plasma membranes in a lipid composition–dependent manner [7,9]. In anionic membranes, DynA and BigDyn induce calcium leakage and membrane permeabilization, whereas in neutral membranes DynA can form ion channel–like pores or undergo direct translocation [8,10,15]. Clinical variants display differential behavior: R6W and R9C show increased membrane insertion, pore stability, resistance to proteolytic degradation, and neurotoxicity compared to WT [13,14,16]. In contrast, the L5S variant exhibits enhanced degradation and reduced membrane-disruptive activity experimentally, despite computational predictions suggesting strong CPP-like behavior [14,16,17].

* Corresponding author. Unit of Biophysics, Department of Biochemistry and Molecular Biology, Facultat de Medicina, Av. Can Domènech s/n, Universitat Autònoma de Barcelona, 08193, Cerdanyola del Vallès, Catalonia, Spain.
E-mail address: alex.peralvarez@uab.cat (A. Peralvarez-Marin).

https://doi.org/10.1016/j.bbrc.2026.154059
Received 15 May 2026; Accepted 28 May 2026
Available online 29 May 2026

This discrepancy between computational and experimental observations highlights the challenges of correlating peptide–membrane interactions across timescales, concentrations, and model systems. To address this gap, we combine Computational Electrophysiology (CompEL) [18], which enables the study of larger peptide–lipid ratios and membrane perturbation under transmembrane potential, with in vitro liposome leakage and aggregation assays. Using this integrated approach, we investigate how membrane composition and sequence variation modulate DynA WT and variant behavior, aiming to establish generalizable principles of peptide–membrane interaction and aggregation.

2. Material and methods

2.1. Computational electrophysiology

CompEL has been used for the computational study of DynA WT and its clinical variants membrane disruption following the same protocol previously used our lab [18]. In brief, double-bilayer systems were generated with CHARMM-GUI [19–21] to accommodate periodic boundary conditions. A transmembrane potential (ΔQ = 16) was applied by asymmetric placement of K^+ and Cl^- ions, followed by adjustment to 150 mM KCl and solvation with TIP3P water. DynA structures were taken from prior work [17], and eight identical peptides were placed in the inner aqueous compartment (protein:lipid ratio 1:32).

Systems were energy-minimized, briefly equilibrated, and simulated for 500 ns in three independent replicas (~20 μs total) using GROMACS with CompEL ion control and the CHARMM36 m force field [22] [23–30]. Three membrane compositions were examined (Table S1): POPC, POPC:PG (7:3), and POPC:PG:CHOL (6:3:1). Trajectories were analyzed in a Jupyter Notebook [31] using GROMACS tools and Matplotlib [32] and structures were visualized in VMD [33].

2.2. Peptides and sample preparation

Peptides used in this work are shown in Table 1. DynA variants were purchased from Pepmic (China) and $A\beta_{1\text{-}42}$ was from JPT (Germany). The peptide concentration was determined by weight or spectrophotometrically by absorbance at 280 nm. DynA variants were dissolved in 10 mM NaPi buffer, pH 7.4, at a stock concentration of 250 μM. $A\beta_{1\text{-}42}$ was prepared at pH 11 (dissolved with 20 mM NaOH to 220 μM, and brought to pH 7.2 prior to kinetic experiments. Liposome leakage experiements were performed at 5 μM and 10 μM peptide concentration for P:L 1:20 and 1:10, respectively.

2.3. Liposome leakage

1-palmitoyl-2-oleoyl-sn-glycero-3-phosphocholine (POPC, Affymetrix, California, USA), 1-Palmitoyl-2-Oleyol-sn-Glycerol-3-[Phosho-rac-(1-glycerol)] (PG, Avanti, Alabama, USA), and cholesterol (Chol, Sigma-Aldrich, Missouri, USA) were dissolved in $CHCl_3$/Methanol (2:1 v/v) solvent to obtain the following mixtures and molar ratios; POPC, POPC:PG, 7:3, and POPC:PG:Chol, 6:3:1. Liposomes were prepared as described previously [34,35]. Briefly, lipid films were prepared by rotary evaporation, hydrated in 10 mM phosphate buffer (pH 7.2) containing 2 mM HPTS, and extruded through polycarbonate membranes (400–100 nm). Vesicle size was confirmed by DLS. Non-encapsulated HPTS was removed by size-exclusion chromatography, and liposomes were adjusted to 100 μM lipid with 5 mM DPX. HPTS fluorescence (λ_exc 420 nm, λ_em 520 nm) was monitored over time following peptide addition (5 or 10 μM). Complete leakage was determined by adding 5 mM Triton X-100, and membrane permeabilization was quantified as the decrease in relative fluorescence.

2.4. Aggregation and hydrophobic surface exposure kinetics

Amyloid assembly and hydrophobic surface exposure were assessed by fluorescence assays using Thioflavin T (ThT; Sigma-Aldrich, Cat. No. T3516) and 4,4′-Dianilino-1,1′-binaphthyl-5,5′-disulfonic acid dipotassium salt (Bis-ANS; Tocris Bioscience, Cat. No. 4434), respectively. ThT aggregation assays were performed as previously described [36]. Briefly, $A\beta_{1-42}$ (10 μM) was incubated alone or with DynA variants at 1:1 and 1:2 M ratios (DynA 10–20 μM) in the presence of 40 μM ThT (λ_exc 440 nm, λ_em 520 nm). Hydrophobic surface exposure was monitored using Bis-ANS (10 μM; λ_exc 380 nm, λ_em 520 nm) under otherwise comparable conditions. All measurements were carried out at 37 °C without shaking using a microplate reader.

For analysis, all raw fluorescence intensities were background-corrected and zero-leveled relative to a probe-only blank (F_{blank}), representing the intensity of ThT or Bis-ANS in buffer alone:

$$Fnorm2 = \frac{Fnorm1 - F0A\beta}{FmaxA\beta - F0A\beta}$$

Samples containing DynA variants in the absence of were expressed as signal fold-change according to this initial normalization. To enable the analytical comparison of the aggregation amplitude (A) as a fold-change relative to the control, a second normalization step was applied to all samples containing $A\beta_{1\text{-}42}$:

$$Fnorm2 = \frac{Fnorm1 - F0A\beta}{FmaxA\beta - F0A\beta}$$

In this step, and represent the initial and maximum fluorescence intensities of the control, respectively, scaling the signal from 0 to 1. The resulting kinetic traces were analyzed using nonlinear regression with a four-parameter sigmoidal Boltzmann equation:

$$F(t) = \frac{A}{1 + exp[r_{max} \times (\tau - t)]}$$

This model allowed for the determination of the plateau amplitude (A), the apparent maximum growth rate (r_{max}), and the aggregation half-time (τ). All reported values represent the mean and standard error (SEM) from at least three independent experiments.

2.5. Data availability

Simulation and analysis files are uploaded at:
https://github.com/APMlab-memb/CompEL_DynAs.git.
Due to file size limitations, simulation trajectories will be shared upon request.

Table 1
Sequence and physico-chemical properties of the peptides used in this research.

Peptide	Primary sequence	MW	Charge	GRAVY Index
$A\beta_{1\text{-}42}$	DAEFRHDSGYEVHHQKLVFFAEDVGSNKGAIIGLMVGGVVIA	4,514.1	−3	0.20
DynA WT	YGGFLRRIRPKLKWDNQ	2147.51	+4	−1.2
DynA L5S	YGGF**S**RRIRPKLKWDNQ	2121.43	+4	−1.5
DynA R6W	YGGFL**W**RIRPKLKWDNQ	2177.54	+3	−1.05
DynA R9C	YGGFLRRI**C**PKLKWDNQ	2094.46	+3	−0.85

3. Results

DynA clinical variants (P:L 1:32) have been simulated in POPC; POPC:PG (7:3), and POPC:PG:CHOL (6:3:1) symmetric bilayer compositions, in the presence of a transmembrane potential. After 500 ns (Fig. 1A), peptides mostly partition in the bilayer, but there are discrete events (Fig. 1B) of peptide insertion and peptide translocation. Thereafter, conformational behavior and secondary structure conversions (Fig. 1C) and specific residue-medaited peptide-lipid interactions (Fig. 1D), for all clinical variants in each lipid bilayer, were respectively assessed and characterized.

Across all three membrane compositions (Fig. 1A and B), interfacial partitioning dominates for all DynA variants. Insertion occurs with less frequency, but higher in POPC, lower in POPC:PG, and hindered in POPC:PG:CHOL. R9C seems to show variant-specific enrichment for insertion in POPC:PG Translocation is rare, but happens for L5S in POPC and for R9C in POPC and POPC:PG, respectively. Secondary structure plots (Fig. 1C) show largely uniform coil/unstructured species across all conditions, confirming DynA remains predominantly unstructured throughout simulations. Sporadic streaks of transient helical or turn structures appear mainly in the N-terminal region and are most visible in POPC:PG (e.g., L5S shows a notable hairpins structure during membrane insertion events) and POPC:PG:CHOL conditions. These transient structured episodes correlate with membrane-inserted states and are absent or minimal in pure POPC, suggesting that anionic lipids (PG) promote brief secondary structure formation upon deeper membrane engagement. Regarding the peptide-lipid contacts, Fig. 1D reveals a clear N-terminal contact signature. In POPC, DynA interacts strongly with the upper leaflet regardless of the variant, and the N-terminal contact signature spans residues 1-14, mediated by both hydrophobic and positively charged residues. In POPC:PG this N-terminal contact signature is restricted to the residues 1-7, and the positively charged residues become more relevant than hydrophobic ones, especially for R6W and R9C where the loss of the Arg is compensated by the neighboring positively charged residues (Fig. 1D). In POPC:PG:CHOL, contact frequencies are globally reduced (shift toward blue), indicating cholesterol dampens membrane association. Variants (L5S, R6W, R9C) show modestly altered contact profiles at the mutated positions relative to WT, but the N-terminal anchor is preserved across variants.

Transient and stable pores are formed during the simulations (Fig. 1A). Pore dimensions extracted from MD simulations (Table S2) reveal a strong membrane composition-dependent effect on DynA-induced bilayer disruption. In POPC, all variants produced comparably large pores (18-23 Å) well above the control (15 Å), consistent with the permissive nature of a pure PC bilayer. Introduction of PG dramatically reduced baseline pore size (control: 0.2 Å), yet R6W and R9C selectively rescued pore formation (5.4 and 7.3 Å, respectively), while WT and L5S remained near control levels, mirroring the insertion events and transient secondary structure observed for these variants in POPC:PG simulations (Fig. 1C). In the cholesterol-containing membrane, the response diverged further, where WT and R9C sustained moderate pore sizes (in the 5 Å range), whereas R6W and L5S were strongly suppressed (<2 Å), indicating that cholesterol selectively neutralizes the pore-forming capacity of specific variants. Together, these data demonstrate that DynA-mediated pore formation is governed by membrane association, but it is also peptide sequence dependent, that is differentially modulated by anionic lipids and cholesterol.

To validate the *in silico* membrane perturbation activity of DynA and its clinical variants variants, we performed fluorescence quenching-based leakage assays using LUVs. Normalized fluorescence was monitored over time, where a decrease in signal represents the leakage and subsequent quenching of the encapsulated HPTS by DPX upon peptide addition at approximately 5 min. In neutral POPC bilayers, all peptides behaved similarly at both 1:20 (Fig. 2A) and 1:10 (Fig. 2B) peptide-to-lipid (P:L) ratios, with a ca. <20% leakage. In these conditions, normalized fluorescence remained above 0.8 until the addition of Triton X-100 at 75 min, which induced total vesicle permeabilization. The introduction of PG significantly sensitized the membranes to peptide-induced disruption (Fig. 2C and D. At a 1:20 ratio (Fig. 2C), moderate leakage was initiated by all peptides (>20%). This effect was markedly amplified at a 1:10 ratio (Fig. 2D), where the R6W and R9C show more rapid and extensive leakage (>50%), with fluorescence dropping up to

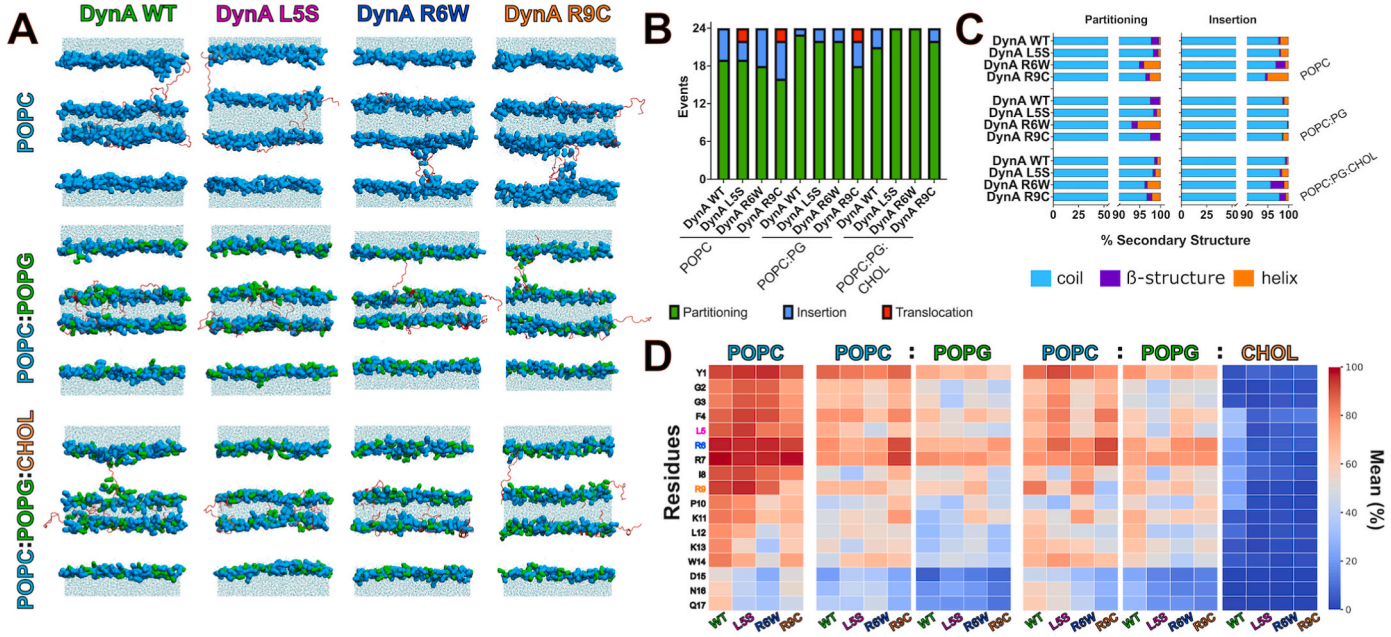

Fig. 1. Membrane interaction behavior of DynA variants across lipid compositions. (A) Representative snapshots from molecular dynamics simulations. Peptides are shown in cartoon representation, and lipids are rendered as surfaces/lines colored by species. **(B)** Quantification and classification of peptide-bilayer interaction events observed over simulation trajectories. **(C)** Average secondary structure changes in the partitioning and insertion events for DynA variants across CompEL trajectories for each variant in different lipid environment. **(D)** Heat map showing residue-level contact frequency (mean %) between DynA variants and lipid bilayers. Rows correspond to residues, and columns represent peptide variants in different lipid models.

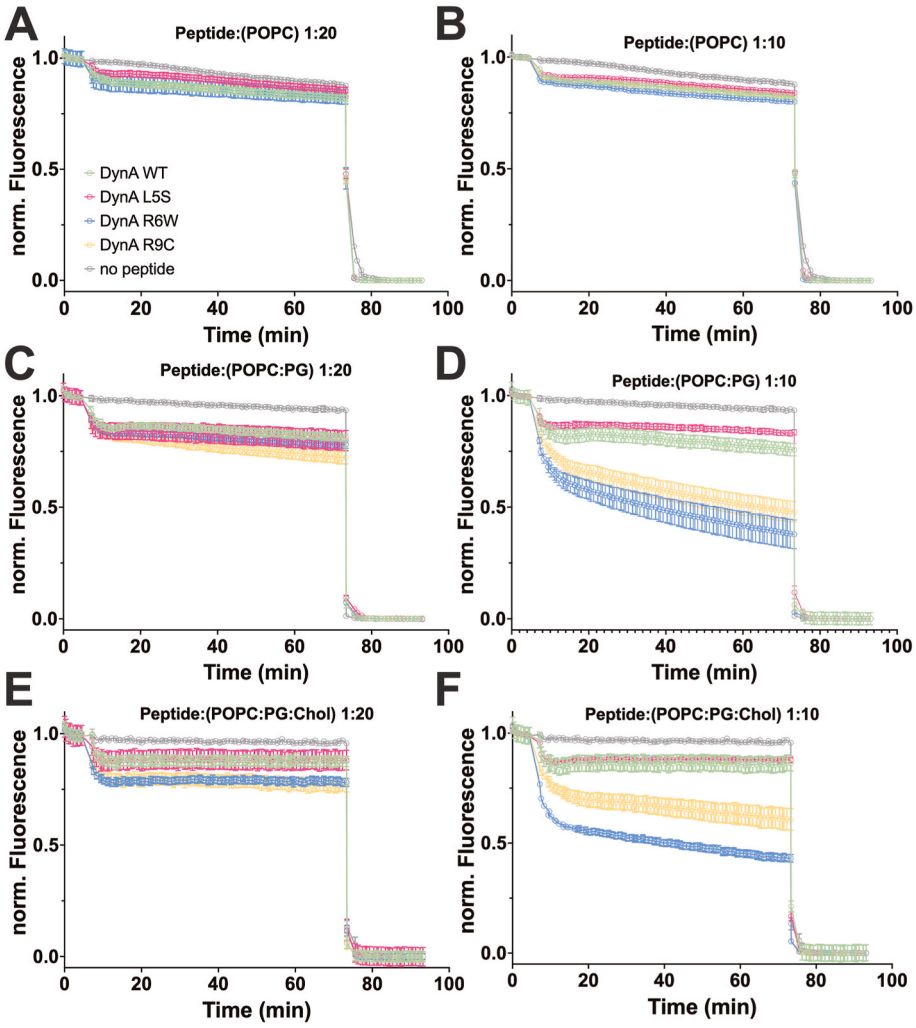

Fig. 2. Liposome leakage assay monitoring membrane permeabilization by DynA variants. Normalized fluorescence intensity is shown over time for the liposome models incubated with DynA peptides at peptide:lipid molar ratios of 1:20 and 1:10. The vertical green drop at ~80 min in every panel represents the addition of detergent (Triton X-100) to fully disrupt all liposomes and establish the baseline fluorescence for normalization. (For interpretation of the references to color in this figure legend, the reader is referred to the Web version of this article.)

~0.4 within 60 min (Table S3).

The inclusion of cholesterol in the membrane (POPC:PG:Chol) modulated the disruptive capacity of the peptides, highlighting differences between the WT, L5S (leakage <20%, Fig. 2E) and the R6W and R9C variants at 1:20 ratio (leakage >20%, Fig. 2E). At the 1:10 the differences between the WT and L5S subgroup are exacerbated in respect to the R6W and R9C subgroup (leakage >20%, Fig. 2E), where both the variants affecting positive residues show larger leakage effects up to ~0.45 (Fig. 2F), but with the extent of leakage slightly attenuated compared to the cholesterol-free system (Fig. 2D). A common activity hierarchy across all active conditions was consistently observed as DynA R6W > DynA R9C > DynA L5S ≈ DynA WT. L5S and WT displayed soft leakage profiles in most panels, regardless of the lipid composition and the P:L ratio of choice (Table S3).

The membrane perturbartion exerted by DynA and the clinical variants, show that purely zwitterionic membranes (POPC) resist disruption, but the introdcution of electrostatic attraction (PG) seems to be required as a primary anchor before hydrophobic deeper insertion can occur.

The CompEL simulation and membrane leakage assays establish that DynA variants disrupt lipid bilayers assuming non-aggregated peptide conditions. Having defined this membrane-active regime, we next examined whether these variants exhibit aggregation-related behaviors in solution, either intrinsically or through interactions with aggregation-prone peptides, by analyzing ordered assembly and hydrophobic surface exposure using fluorescence-based aggregation assays.

Ordered assembly and hydrophobic surface exposure were monitored using Thioflavin T (ThT) and Bis-ANS fluorescence, respectively (Fig. 3). Kinetic parameters were obtained by sigmoidal fitting, yielding the amplitude (A), apparent rate constant (r_{max}), and half-time (τ) for each condition (Table S4). DynA variants alone showed negligible ThT signal (Fig. 3A), indicating the absence of spontaneous ordered aggregation. $A\beta_{1\text{-}42}$ alone displayed a sigmoidal aggregation profile (Fig. 3B) with $A = 0.9 \pm 0.0$ and $\tau = 284.3 \pm 5.7$ min.

Addition of DynA WT at a 1:2 M ratio reduced the final ThT plateau ($A = 0.7 \pm 0.0$) and shortened the half-time ($\tau = 166.6 \pm 4.0$ min), indicating modulation of fibril accumulation. The DynA L5S variant strongly altered $A\beta_{1\text{-}42}$ aggregation behavior (Fig. 3C). At a 1:2 ratio, L5S increased the ThT amplitude to $A = 4.0 \pm 0.4$ and accelerated kinetics ($\tau = 10.0 \pm 14.8$ min). The R6W and R9C variants retained sigmoidal kinetics comparable to $A\beta_{1\text{-}42}$ alone (Fig. 3D and E). R6W (1:2) yielded $A = 1.0 \pm 0.0$, while R9C (1:2) showed a moderate increase in amplitude ($A = 1.3 \pm 0.0$) with $\tau = 232.7 \pm 10.6$ min.

Bis-ANS assays revealed distinct hydrophobic co-aggregation behavior (Fig. 3F–J). DynA WT alone showed a slightly decreasing signal. L5S and R6W alone exhibited rapid fluorescence decay. R9C

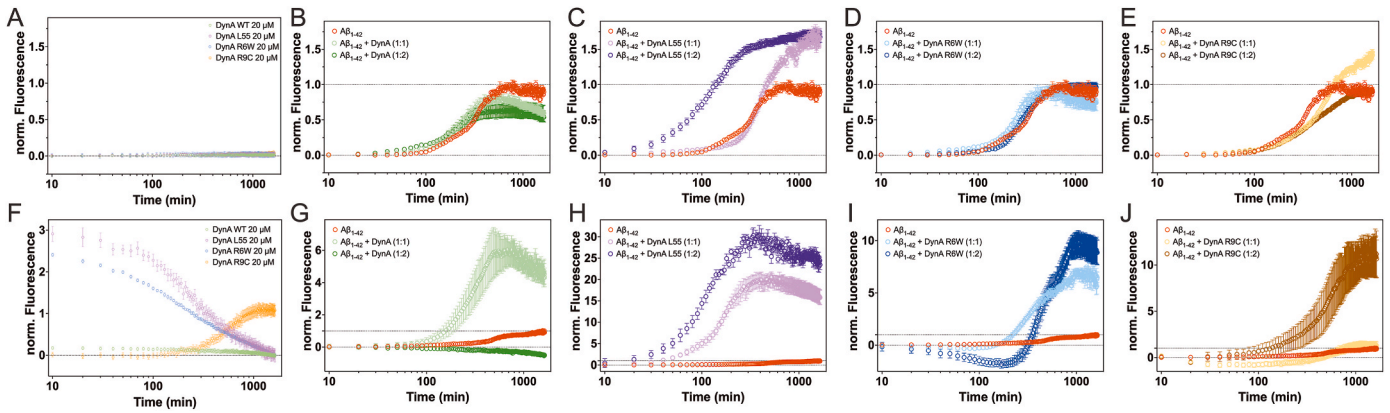

Fig. 3. Kinetic modulation of aggregation and hydrophobic surface exposure by DynA variants. The aggregation of $A\beta_{1-42}$ (10 μM) was monitored in the presence of various DynA variants at molar ratios of 1:1 (10 μM) and 1:2 (20 μM) over 1,500 min. (A–E) Ordered assembly kinetics monitored by Thioflavin T (ThT) fluorescence. (A) Basal ThT fluorescence of DynA variants alone (20 μM). (B–E) Co-incubation of $A\beta_{1-42}$ (red circles) with DynA WT (B), L5S (C), R6W (D), and R9C (E). (F–J) Hydrophobic surface exposure monitored by Bis-ANS fluorescence. (F) Basal Bis-ANS fluorescence of DynA variants alone (20 μM). WT exhibits a slightly decreasing slope, L5S and R6W show exponential decay, and R9C displays independent sigmoidal growth. (G–J) Co-incubation of with DynA WT (G), L5S (H), R6W (I), and R9C (J). For kinetic parameters refer to Table S4. The dotted line in panels B-E and G-J shows the $A\beta_{1-42}$ normalized maximum fluorescence value as a reference (value of 1.0) for comparison. All reported values represent the mean and standard error (SEM) from at least three independent experiments. (For interpretation of the references to color in this figure legend, the reader is referred to the Web version of this article.)

alone displayed a sigmoidal increase, consistent with hydrophobic self-assembly. In the presence of $A\beta_{1-42}$, DynA WT produced low hydrophobic exposure (Fig. 3G), with A = 5.2 ± 0.2 at a 1:1 ratio and insufficient signal for fitting at 1:2. Clinical variants induced pronounced hydrophobic species. L5S (1:2) reached a Bis-ANS amplitude of 28.2 ± 1.9, compared to 1.2 ± 0.1 for $A\beta_{1-42}$ alone, corresponding to a ~24-fold increase (Fig. 3H). The half-time was τ = 90.3 ± 6.9 min, later than the ThT transition. R6W and R9C at 1:2 reached amplitudes of 11.2 ± 0.2 and 11.9 ± 0.1, with delayed half-times of 479.7 ± 6.1 min and 444.9 ± 5.0 min, respectively (Fig. 3I and J).

Across all conditions, ThT amplitudes remained within a narrow range (A ≈ 0.7–4.0), while Bis-ANS amplitudes varied widely for the mutant variants (A ≈ 11.2–28.2). This indicates dissociation between ordered fibril formation and hydrophobic surface exposure, consistent with the accumulation of non-fibrillar, hydrophobic co-aggregates.

4. Discussion

This study examines how sequence variations in Dynorphin A (DynA), including the wild-type peptide and the SCA23-associated variants L5S, R6W, and R9C, influence peptide structure, membrane interaction, and aggregation behavior under controlled biophysical conditions [11,13]. By combining CompEL simulations with membrane leakage and fluorescence-based aggregation assays, we analyze general principles governing how short, highly cationic peptides interact with lipid bilayers and aggregation-prone partners such as amyloid-β (Aβ) [14,37]. While these variants are clinically observed in SCA23, the present work focuses on fundamental peptide–membrane and peptide–peptide interactions rather than on disease mechanisms.

DynA displays pronounced conformational plasticity, adopting an N-terminal α-helical structure upon membrane association, consistent with previous structural studies [14,15]. The L5S, R6W, and R9C substitutions reduce this membrane-induced helicity, demonstrating that single-residue changes can substantially disrupt local secondary structure in membrane-mimetic environments [14,35]. These findings underscore the sensitivity of amphipathic helices to sequence perturbations and highlight how residue chemistry modulates membrane-facing conformations.

At submicellar concentrations, DynA and its variants form aggregated species that retain predominantly α-helical character, in contrast to the β-sheet–rich assemblies typical of many amyloid-forming peptides [38]. Membrane leakage assays revealed a consistent hierarchy of bilayer perturbation (R6W > R9C > WT > L5S), reflecting the combined contributions of electrostatic membrane recruitment and mutation-dependent insertion depth [13]. CompEL simulations support an accumulation-dependent interaction mode in compositionally complex membranes, leading to transient proteolipidic defects rather than stable pore formation, in agreement with established models for amphipathic, cationic peptides [8,10,39].

The greatest divergence between simulation and experiment was observed for the L5S variant. Although computational models predicted strong membrane association, experimental leakage was minimal [13,35]. This highlights the importance of peptide stability and solution behavior, as L5S is more rapidly degraded than other variants, reducing its effective membrane engagement [14].

Co-aggregation experiments with Aβ1–42 further illustrate how DynA variants influence aggregation behavior. Thioflavin T assays showed limited effects on ordered fibril kinetics, consistent with previous observations [37]. In contrast, Bis-ANS measurements revealed substantial increases in hydrophobic surface exposure, particularly for L5S, indicating the formation of non-fibrillar, amorphous co-assemblies. This uncoupling of ordered assembly from hydrophobic exposure reinforces the view that aggregation pathways can be redirected without enhancing fibrillization.

Overall, this work delineates how specific sequence features of DynA-derived peptides govern secondary structure stability, membrane interaction modes, and aggregation behavior. The results provide a biophysical framework for understanding how modest sequence perturbations modulate peptide association with lipid bilayers and influence aggregation pathways during co-assembly, offering general insights applicable to amphipathic, membrane-active peptides and aggregation-prone systems more broadly [14,37].

Declaration of AI-assisted technologies in the manuscript preparation process

During the preparation of this work the author(s) used COPILOT in order to improve the readability of the content. After using this tool/service, the authors reviewed and edited the content as needed and take full responsibility for the content of the published article.

CRediT authorship contribution statement

Mohsen Habibnia: Formal analysis, Investigation, Writing – review

& editing. **Eric Catalina-Hernandez:** Formal analysis, Investigation, Writing – review & editing. **Ramon Barnadas-Rodríguez:** Funding acquisition, Resources, Supervision, Writing – review & editing. **Alex Peralvarez-Marin:** Conceptualization, Formal analysis, Funding acquisition, Resources, Supervision, Writing – original draft, Writing – review & editing.

Declaration of competing interest

The authors declare no competing interests.

Acknowledgements

Authors acknowledge financial support by the Spanish Government Grant MCIN/AEI/10.13039/501100011033 PID2020-120222 GB-I00 (to A.P.-M.), PID2021-123682OB-I00 (to R.B.-R), and Universitat Autònoma de Barcelona predoctoral fellowship (B21P0033 to E.C.-H.).

Appendix A. Supplementary data

Supplementary data to this article can be found online at https://doi.org/10.1016/j.bbrc.2026.154059.

References

[1] G.Y. Bakalkin, A.B. Rakhmaninova, V.K. Akparov, A.A. Volodin, V.V. Ovchinnikov, R.A. Sarkisyan, Amino acid sequence pattern in the regulatory peptides, Int. J. Pept. Protein Res. 38 (1991) 505–510, https://doi.org/10.1111/j.1399-3011.1991.tb01533.x.

[2] T. Yakovleva, Z. Marinova, A. Kuzmin, N.G. Seidah, V. Haroutunian, L. Terenius, G. Bakalkin, Dysregulation of dynorphins in Alzheimer disease, Neurobiol. Aging 28 (2007) 1700–1708, https://doi.org/10.1016/j.neurobiolaging.2006.07.002.

[3] W. Fischli, A. Goldstein, M.W. Hunkapiller, L.E. Hood, Two “big” dynorphins from porcine pituitary, Life Sci. 31 (1982) 1769–1772, https://doi.org/10.1016/0024-3205(82)90206-5.

[4] W. Fischli, A. Goldstein, M.W. Hunkapiller, L.E. Hood, Isolation and amino acid sequence analysis of a 4,000-dalton dynorphin from porcine pituitary, Proc. Natl. Acad. Sci. 79 (1982) 5435–5437, https://doi.org/10.1073/pnas.79.17.5435.

[5] C. Ménard, H. Herzog, C. Schwarzer, R. Quirion, Possible role of dynorphins in alzheimer's disease and age-related cognitive deficits, Neurodegener. Dis. 13 (2014) 82–85, https://doi.org/10.1159/000353848.

[6] K.F. Hauser, J.K. Foldes, C.S. Turbek, Dynorphin A (1–13) neurotoxicity in vitro: opioid and non-opioid mechanisms in Mouse Spinal cord neurons, Exp. Neurol. 160 (1999) 361–375, https://doi.org/10.1006/exnr.1999.7235.

[7] Z. Marinova, V. Vukojević, S. Surcheva, T. Yakovleva, G. Cebers, N. Pasikova, I. Usynin, L. Hugonin, W. Fang, M. Hallberg, D. Hirschberg, T. Bergman, Ü. Langel, K.F. Hauser, A. Pramanik, J.V. Aldrich, A. Gräslund, L. Terenius, G. Bakalkin, Translocation of dynorphin neuropeptides across the plasma membrane, J. Biol. Chem. 280 (2005) 26360–26370, https://doi.org/10.1074/jbc.M412494200.

[8] L. Hugonin, V. Vukojević, G. Bakalkin, A. Gräslund, Membrane leakage induced by dynorphins, FEBS Lett. 580 (2006) 3201–3205, https://doi.org/10.1016/j.febslet.2006.04.078.

[9] L. Hugonin, V. Vukojević, G. Bakalkin, A. Gräslund, Calcium influx into phospholipid vesicles caused by dynorphin neuropeptides, Biochim. Biophys. Acta Biomembr. 1778 (2008) 1267–1273, https://doi.org/10.1016/j.bbamem.2008.02.003.

[10] L.M. Alvero-Gonzalez, D. Aurora Perini, M. Queralt-Martín, A. Perálvarez-Marín, C. Viñas, A. Alcaraz, Probing electrophysiological activity of amphiphilic Dynorphin A in planar neutral membranes reveals both ion channel-like activity and neuropeptide translocation, Bioelectrochemistry 154 (2023) 108527, https://doi.org/10.1016/j.bioelechem.2023.108527.

[11] G. Bakalkin, H. Watanabe, J. Jezierska, C. Depoorter, C. Verschuuren-Bemelmans, I. Bazov, K.A. Artemenko, T. Yakovleva, D. Dooijes, B.P.C. Van de Warrenburg, R. A. Zubarev, B. Kremer, P.E. Knapp, K.F. Hauser, C. Wijmenga, F. Nyberg, R. J. Sinke, D.S. Verbeek, Prodynorphin mutations cause the neurodegenerative disorder Spinocerebellar Ataxia type 23, Am. J. Hum. Genet. 87 (2010) 593–603, https://doi.org/10.1016/j.ajhg.2010.10.001.

[12] F. Wu, X. Wang, X. Li, H. Teng, T. Tian, J. Bai, Spinocerebellar ataxia type 23 (SCA23): a review, J. Neurol. 268 (2021) 4630–4645, https://doi.org/10.1007/s00415-020-10297-5.

[13] F. Madani, M.M. Taqi, S.K.T.S. Wärmländer, D.S. Verbeek, G. Bakalkin, A. Gräslund, Perturbations of model membranes induced by pathogenic dynorphin A mutants causing neurodegeneration in human brain, Biochem. Biophys. Res. Commun. 411 (2011) 111–114, https://doi.org/10.1016/j.bbrc.2011.06.105.

[14] C.J.L.M. Smeets, J. Zmorzyńska, M.N. Melo, A. Stargardt, C. Dooley, G. Bakalkin, J. McLaughlin, R.J. Sinke, S.-J. Marrink, E. Reits, D.S. Verbeek, Altered secondary structure of Dynorphin A associates with loss of opioid signalling and NMDA-mediated excitotoxicity in SCA23, Hum. Mol. Genet. (2016), https://doi.org/10.1093/hmg/ddw130 ddw130.

[15] J. Lind, A. Gräslund, L. Mäler, Membrane interactions of dynorphins, Biochemistry 45 (2006) 15931–15940, https://doi.org/10.1021/bi061199g.

[16] J. Björnerås, A. Gräslund, L. Mäler, Membrane interaction of disease-related dynorphin A variants, Biochemistry 52 (2013) 4157–4167, https://doi.org/10.1021/bi4004205.

[17] E. Catalina-Hernandez, M. Lopez-Martin, M. Aguilella-Arzo, A. Peralvarez-Marin, Membrane disruption potential of endogenous opioid neuropeptide Dynorphin A and related clinical variants, Int. J. Biol. Macromol. 316 (2025) 144567, https://doi.org/10.1016/j.ijbiomac.2025.144567.

[18] E. Catalina-Hernandez, M. Aguilella-Arzo, M. Lopez-Martin, A. Peralvarez-Marin, Understanding cell-penetrating peptide mechanisms using computational electrophysiology simulations. https://doi.org/10.1002/pro.70536, 2026.

[19] S. Jo, T. Kim, V.G. Iyer, W. Im, CHARMM-GUI: a web-based graphical user interface for CHARMM, J. Comput. Chem. 29 (2008) 1859–1865, https://doi.org/10.1002/jcc.20945.

[20] E.L. Wu, X. Cheng, S. Jo, H. Rui, K.C. Song, E.M. Dávila-Contreras, Y. Qi, J. Lee, V. Monje-Galvan, R.M. Venable, J.B. Klauda, W. Im, CHARMM-GUI Membrane Builder toward realistic biological membrane simulations, J. Comput. Chem. 35 (2014) 1997–2004, https://doi.org/10.1002/jcc.23702.

[21] J. Lee, X. Cheng, J.M. Swails, M.S. Yeom, P.K. Eastman, J.A. Lemkul, S. Wei, J. Buckner, J.C. Jeong, Y. Qi, S. Jo, V.S. Pande, D.A. Case, C.L.I.I.I. Brooks, A.D. Jr. MacKerell, J.B. Klauda, W. Im, CHARMM-GUI input generator for NAMD, GROMACS, AMBER, OpenMM, and CHARMM/OpenMM simulations using the CHARMM36 additive force field, J. Chem. Theor. Comput. 12 (2016) 405–413, https://doi.org/10.1021/acs.jctc.5b00935.

[22] C. Kutzner, H. Grubmüller, B.L. De Groot, U. Zachariae, Computational electrophysiology: the molecular dynamics of ion channel permeation and selectivity in atomistic detail, Biophys. J. 101 (2011) 809, https://doi.org/10.1016/J.BPJ.2011.06.010.

[23] H. Bekker, H. Berendsen, E. Dijkstra, S. Achterop, R. VonDrumen, D. VanDerSpoel, A. Sijbers, H. Keegstra, B. Reitsma, M. Renardus, Gromacs - a parallel computer for molecular dynamics simulations, PHYSICS COMPUTING 92 (1993) 252–256.

[24] D. Van Der Spoel, E. Lindahl, B. Hess, G. Groenhof, A.E. Mark, H.J.C. Berendsen, GROMACS: fast, flexible, and free, J. Comput. Chem. 26 (2005) 1701–1718, https://doi.org/10.1002/JCC.20291.

[25] H.J.C. Berendsen, D. van der Spoel, R. van Drunen, GROMACS: a message-passing parallel molecular dynamics implementation, Comput. Phys. Commun. 91 (1995) 43–56, https://doi.org/10.1016/0010-4655(95)00042-E.

[26] S. Páll, M.J. Abraham, C. Kutzner, B. Hess, E. Lindahl, Tackling exascale software challenges in molecular dynamics simulations with GROMACS, Lect. Notes Comput. Sci. 8759 (2015) 3–27, https://doi.org/10.1007/978-3-319-15976-8_1.

[27] E. Lindahl, B. Hess, D. van der Spoel, Gromacs 3.0: a package for molecular simulation and trajectory analysis, J. Mol. Model. 7 (2001) 306–317, https://doi.org/10.1007/S008940100045/METRICS.

[28] M.J. Abraham, T. Murtola, R. Schulz, S. Páll, J.C. Smith, B. Hess, E. Lindah, GROMACS: high performance molecular simulations through multi-level parallelism from laptops to supercomputers, SoftwareX 1–2 (2015) 19–25, https://doi.org/10.1016/J.SOFTX.2015.06.001.

[29] B. Hess, C. Kutzner, D. Van Der Spoel, E. Lindahl, Gromacs 4: algorithms for highly efficient, Load-Balanced, and scalable molecular simulation, J. Chem. Theor. Comput. 4 (2008) 435–447, https://doi.org/10.1021/CT700301Q.

[30] S. Pronk, S. Páll, R. Schulz, P. Larsson, P. Bjelkmar, R. Apostolov, M.R. Shirts, J. C. Smith, P.M. Kasson, D. Van Der Spoel, B. Hess, E. Lindahl, Gromacs 4.5: a high-throughput and highly parallel open source molecular simulation toolkit, Bioinformatics 29 (2013) 845–854, https://doi.org/10.1093/BIOINFORMATICS/BTT055.

[31] J.D. Hunter, Matplotlib: a 2D graphics environment, Comput. Sci. Eng. 9 (2007) 90–95, https://doi.org/10.1109/MCSE.2007.55.

[32] T. Kluyver, B. Ragan-Kelley, F. Pérez, B. Granger, M. Bussonnier, J. Frederic, K. Kelley, J. Hamrick, J. Grout, S. Corlay, P. Ivanov, D. Avila, S. Abdalla, C. Willing, J. development team, T. Kluyver, B. Ragan-Kelley, F. Pérez, B. Granger, M. Bussonnier, J. Frederic, K. Kelley, J. Hamrick, J. Grout, S. Corlay, P. Ivanov, D. Avila, S. Abdalla, C. Willing, J. development team, F. Loizides, B. Scmidt, Jupyter Notebooks – a publishing format for reproducible computational workflows, in: F. Loizides, B. Scmidt (Eds.), 20th International Conference on Electronic Publishing (01/01/16), IOS Press, 2016, pp. 87–90, https://doi.org/10.3233/978-1-61499-649-1-87.

[33] W. Humphrey, A. Dalke, K. Schulten, VMD: visual molecular dynamics, J. Mol. Graph. 14 (1996) 33–38, https://doi.org/10.1016/0263-7855(96)00018-5.

[34] M.J. Gomara, Y. Perez, J.P. Martinez, R. Barnadas-Rodriguez, A. Schultz, H. von Briesen, A. Peralvarez-Marin, A. Meyerhans, I. Haro, Peptide assembly on the membrane determines the HIV-1 inhibitory activity of dual-targeting fusion inhibitor peptides, Sci. Rep. 9 (2019) 3257, https://doi.org/10.1038/s41598-019-40125-4.

[35] M. Habibnia, E. Catalina-Hernandez, M. Cabrerizo-Idiazabal, R. Barnadas-Rodríguez, M. Lopez-Martin, A. Peralvarez-Marin, Biophysical analysis of angiotensin <scp>II</scp> and amyloid-β cross-interaction in aggregation and membrane disruption, FEBS Lett. 600 (2026) 109–118, https://doi.org/10.1002/1873-3468.70185.

[36] M. Habibnia, E. Catalina-Hernandez, M. Lopez-Martin, D. Masnou-Sanchez, A. Peralvarez-Marin, Decoding the molecular and structural determinants of the neurokinin A and Aβ1-42 peptide cross-interaction in the amyloid cascade pathway, iScience 27 (2024) 111187, https://doi.org/10.1016/j.isci.2024.111187.

[37] L. Gallego-Villarejo, C. Wallin, S. Król, J. Enrich-Bengoa, A. Suades, M. Aguilella-Arzo, M.J. Gomara, I. Haro, S. Wärmlander, F.J. Muñoz, A. Gräslund, A. Perálvarez-Marín, Big dynorphin is a neuroprotector scaffold against amyloid β-peptide aggregation and cell toxicity, Comput. Struct. Biotechnol. J. 20 (2022) 5672–5679, https://doi.org/10.1016/j.csbj.2022.10.014.

[38] L. Hugonin, A. Barth, A. Gräslund, A. Perálvarez-Marín, Secondary structure transitions and aggregation induced in dynorphin neuropeptides by the detergent sodium dodecyl sulfate, Biochim. Biophys. Acta Biomembr. 1778 (2008) 2580–2587, https://doi.org/10.1016/j.bbamem.2008.07.011.

[39] D.A. Perini, M. Aguilella-Arzo, A. Alcaraz, A. Perálvarez-Marín, M. Queralt-Martín, Dynorphin A induces membrane permeabilization by formation of proteolipidic pores. Insights from electrophysiology and computational simulations, Comput. Struct. Biotechnol. J. 20 (2022) 230–240, https://doi.org/10.1016/j.csbj.2021.12.021.